Bachelor Research Project

Atomic-Scale Magnetic and Structural Response to Vacancies in BCC Iron: A Density Functional Theory Study

Author:
Yuval Rossen, S5322197

Supervisors:
Prof. Dr. Ir. E. van der Giessen
Prof. Dr. Ir. F. Maresca

Faculty of Science and Engineering
University of Groningen
Groningen, the Netherlands
July 2025

Abstract

Understanding how vacancies reshape ferromagnetic iron is essential for modeling diffusion, creep, and irradiation damage in steels. Here we present a density-functional-theory investigation of a single vacancy in body-centered-cubic (bcc) iron, performed in a 54-atom supercell with a validated k-point mesh. Formation energies, magnetic moment maps, and displacement fields were obtained through simultaneous electronic and structural relaxation, using both PAW and ultrasoft pseudopotentials. We find a vacancy formation energy of 2.33 ± 0.05 eV; first-shell atoms relax inward by 3% and increase their magnetic moments by 10%, indicating strong short-range magneto-structural coupling. Magnetic and elastic perturbations decay with power-law behavior, confirming that finite-size effects dominate residual errors rather than numerical convergence. This benchmark supports the development of spin-lattice machine-learning potentials and aligns with the upper range of positron-annihilation measurements, demonstrating that accurate vacancy energetics require treating structural and magnetic degrees of freedom on equal footing.

List of Abbreviations

- Å – Ångström (10^{-10} meters)
- BCC – Body-Centered Cubic
- DFT – Density Functional Theory
- DLM – Disordered Local Moment
- DOS – Density of States
- ecutrho – Energy cutoff for charge density
- ecutwfc – Energy cutoff for wavefunctions
- E_F – Fermi Energy
- eV – Electron Volt
- FM – Ferromagnetic
- GGA – Generalized Gradient Approximation
- HPC – High Performance Computing
- K – Kelvin (temperature unit)
- MP – Materials Project
- MPI – Message Passing Interface
- MV – Marzari–Vanderbilt (smearing scheme)
- NM – Non-Magnetic
- PAW – Projector Augmented Wave
- PBE – Perdew–Burke–Ernzerhof (GGA functional)
- QE – Quantum ESPRESSO
- Ry – Rydberg (unit of energy)
- SCF – Self-Consistent Field
- SSA – Symmetry-constrained Spin Averaging
- UPF – Unified Pseudopotential Format
- USPP – Ultrasoft Pseudopotential
- μ_B – Bohr Magneton

Contents

List of Abbreviations **2**

Acknowledgements **4**

1 Introduction **2**

2 Theoretical Background **3**
2.1 The Crystalline State and its Imperfections 3
2.2 Magnetism in Body-Centered Cubic Iron 4
2.3 Magneto-Structural Coupling in Iron 5
2.4 Defect-Induced Structural and Magnetic Response 7
2.4.1 Structural Relaxation Around Point Defects 7
2.4.2 Magnetic Perturbations Around Defects 9

3 Computational Methodology **10**
3.1 First-Principles Framework 10
3.2 Convergence and Validation 10
3.2.1 Energy Cutoffs 10
3.2.2 K-point Sampling 11
3.2.3 Pseudopotential Validation 12
3.3 Computational Parameters 13
3.4 Defect Supercell and Calculation Procedure 14
3.4.1 Supercell Construction 14
3.4.2 Magnetic State Considerations 14
3.4.3 Relaxation Procedure 15
3.4.4 Vacancy Formation Energy Calculation 15

4 Results and Discussion **16**
4.1 Vacancy Formation Energies 16
4.2 Magnetic Moment Enhancement 17
4.3 Structural Relaxation Patterns 18
4.4 Pseudopotential Consistency 20
4.5 Error Analysis and Uncertainty Quantification 20

5 Conclusion **22**

References **23**

Appendix **26**
Appendix A: Quantum ESPRESSO Input Files 26
Appendix B: Convergence Test Data 30
Appendix C: Data Processing Scripts 30
Appendix D: Computational Details 35
Appendix E: Code and Data Availability 35

Acknowledgements

I would like to express my sincere gratitude to the individuals and institutions who made this research possible. First and foremost, I thank my supervisors, Erik van der Giessen and Francesco Maresca, for their invaluable guidance, support, and expertise throughout this project. Their insights into computational materials science and constructive feedback were instrumental in shaping this work. I am also grateful to Lei Zhang for his advice on specific computational approaches, which significantly contributed to the methodology employed in this study. I thank the Faculty of Science and Engineering at the University of Groningen for providing access to the Hábrók high-performance computing cluster, without which the density functional theory calculations presented here would not have been feasible. In developing analysis scripts, I used GitHub Copilot and ChatGPT for debugging assistance. Finally, I would like to thank my family and friends for their encouragement and support during my studies.

1 Introduction

Steel production now exceeds 1.9 billion tonnes per year [1], and iron, the primary constituent of steel, is the most-consumed metal worldwide. The mechanical performance of steel-based infrastructure ultimately depends on the behaviour of crystalline defects, such as dislocations and vacancies, in body-centred-cubic (bcc) α-Fe [2]. Understanding the atomic-scale behavior of iron, particularly how defects influence its properties, is therefore crucial for developing stronger, more durable steels and optimizing their performance in critical applications.

In bcc iron, magnetic and structural properties are strongly coupled, producing defect behaviors that remain fundamentally challenging to understand [3]. When an iron atom is removed to form a vacancy, the perturbation extends well beyond the missing atom and its broken bonds [4]. The local magnetic moments rearrange in complex patterns that remain poorly understood despite their critical role in diffusion, mechanical properties, and phase stability of steels.

Previous studies have calculated vacancy formation energies in iron, yielding values between 1.8 and 2.4 eV compared to experimental measurements near 2.0 eV [5], [6]. This scatter of 0.6 eV, large enough to significantly affect predicted diffusion rates and creep behavior, largely stems from inconsistent treatment of magnetic effects [7]–[9]. However, this energy-centric approach overlooks the rich spatial physics of magnetic moment redistribution around defects. This includes phenomena such as the range and decay behavior of magnetic perturbations, the potential asymmetry in moment enhancement versus suppression, the three-dimensional anisotropy of magnetic response, and most importantly, the feedback mechanisms between local moment changes and atomic displacements. Theoretical work suggests that atoms neighboring a vacancy should enhance their magnetic moments due to reduced coordination [3], but quantitative three-dimensional mapping of these magnetic perturbations remains absent from the literature. Without this spatial information, we cannot understand how magnetic and structural relaxations couple at the atomic scale, nor can we develop accurate models for magnetic materials containing defects.

We address this gap through systematic density functional theory calculations that map both the energetics and the three-dimensional magnetic structure around vacancies in bcc iron. Crucially, we perform all calculations in the ferromagnetic state, where all atomic magnetic moments align parallel, at its equilibrium lattice parameter of 2.868 Å, ensuring physically meaningful results that avoid the artificial mechanical instabilities present in non-magnetic bcc iron calculations. Our calculations reveal a vacancy formation energy of 2.33 ± 0.05 eV with distinct magnetic enhancement of approximately 10% on first-neighbor atoms, localized within a single coordination shell. This magnetic perturbation couples directly to structural relaxation: the same atoms that enhance their moments also relax inward by 3%, providing the first quantitative demonstration of the strong feedback between magnetic and structural degrees of freedom in defective iron.

2 Theoretical Background

2.1 The Crystalline State and its Imperfections

The theoretical physicist's perfect crystal, an infinite periodic array of atoms in flawless repetition, represents a mathematical idealization that nature never achieves. Real materials contain a hierarchy of imperfections that govern their mechanical, thermal, and electronic properties [2]. Among these imperfections, point defects, specifically vacancies, play an important role in determining diffusion rates, mechanical strength, and phase stability [2], [10]. Understanding vacancy behavior is especially important in magnetic materials like iron, where the combination of electronic structure and atomic arrangement has a strong influence on defect energetics [7].

The body-centered cubic (bcc) structure represents one of the fundamental metallic crystal structures. In bcc, atoms occupy the corners of a cubic unit cell plus the cell center, as illustrated in Figure 1. Each atom is surrounded by eight nearest neighbors at a distance of $\sqrt{3}a/2$, yielding a coordination number of 8 [11]. Six second-nearest neighbors lie at distance a along the cube edges.

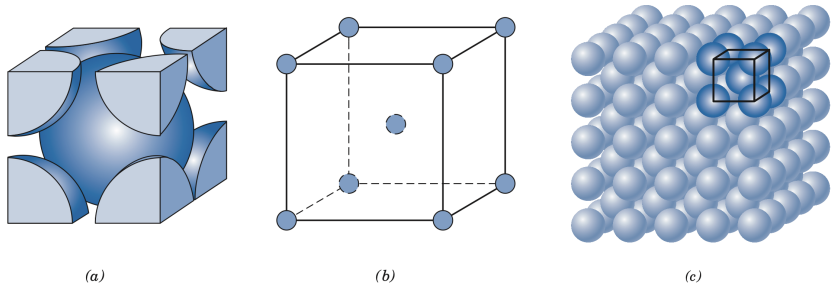

Figure 1: Body-centered cubic (bcc) crystal structure of iron. (a) Cutaway view showing the central atom within the cubic unit cell. (b) Wireframe representation of the bcc unit cell with eight corner atoms and one central atom. (c) Extended bcc lattice showing multiple unit cells, with one unit cell highlighted. Retrieved from [12].

At ambient conditions, α-iron adopts the bcc structure with lattice parameter $a = 2.8665$ Å [13]. This structure persists up to 1185 K, where iron transforms to the face-centered cubic (fcc) γ-phase. The bcc structure's lower packing efficiency compared to fcc (0.74 versus 0.68) might seem energetically unfavorable [11]. However, as section 2.2 will reveal, magnetic exchange interactions in iron stabilize the more open bcc arrangement by favoring larger atomic volumes that enhance magnetic moment formation [14].

Perfect crystalline order exists only as a theoretical construct. Even at 0K, quantum zero-point motion introduces fluctuations from ideal atomic positions [11]. At finite temperatures, thermal energy creates various defects that disrupt periodicity. Point defects, localized disruptions affecting only single lattice sites and their immediate surroundings, represent the simplest class of crystal imperfections [2]. Three primary types of point defects occur in elemental crystals: vacancies (unoccupied lattice sites where atoms are missing), self-interstitials (host atoms occupying non-lattice positions between regular sites), and substitutional impurities (foreign atoms replacing host atoms at lattice sites).

In thermal equilibrium at temperature T, the vacancy concentration follows

$$\frac{n_v}{N} = \exp\left(-\frac{E_f^v}{k_B T}\right) \tag{1}$$

where n_v is the number of vacancies, N is the total number of lattice sites, E_f^v is the vacancy formation energy, and k_B is Boltzmann's constant [10]. For typical metals with $E_f^v \sim 1$ eV, this yields equilibrium concentrations of 10^{-5} at the melting point and 10^{-17} at room temperature. Note that iron has a higher formation energy of $\sim$2 eV, resulting in equilibrium concentrations of approximately 10^{-6} at its melting point (1811 K) and 10^{-34} at room temperature.

This formation energy E_f^v represents the fundamental quantity that density functional theory calculations seek to determine. However, in iron, this seemingly straightforward energy calculation can be complex. The energy required to create a vacancy depends dramatically on whether the iron is treated as magnetic or non-magnetic, with differences that can exceed 0.5 eV, a massive discrepancy in the context of defect thermodynamics [7]. This dependence on magnetic state raises the question: what is it about iron's magnetism that so profoundly affects its defect properties? To answer this, we must first understand the unique nature of ferromagnetism in body-centered cubic iron and how it emerges from the collective behavior of itinerant d-electrons.

2.2 Magnetism in Body-Centered Cubic Iron

Below the Curie temperature of 1043 K, iron exhibits ferromagnetic ordering where atomic magnetic moments align parallel to produce a net magnetization [15]. This magnetism is not only an additional property of the material but rather an integral part of what makes iron adopt and maintain its body-centered cubic structure at room temperature [16].

The origin of magnetism in iron fundamentally different from that of magnetic insulators. While insulators typically have localized magnetic moments bound to specific atomic sites, iron's magnetism arises from its itinerant 3d electrons that simultaneously participate in metallic bonding and carry magnetic moments [16]. These electrons form energy bands instead of discrete atomic levels, with the 3d band being partially filled. The Stoner model provides the theoretical framework for understanding this itinerant ferromagnetism [16]. According to this model, ferromagnetism emerges when the energy gain from aligning electron spins exceeds the kinetic energy cost of redistributing electrons between spin-up and spin-down bands.

The condition for ferromagnetic instability is described by the Stoner criterion as follows:

$$I \cdot n(E_F) > 1 \tag{2}$$

where I is the Stoner exchange parameter (approximately 0.9 eV for iron) and $n(E_F)$ is the density of states at the Fermi level per atom (states/eV/atom), making the product dimensionless [16]. Iron satisfies this criterion because its narrow 3d bands create a high density of states near the Fermi energy. When ferromagnetism develops, the exchange interaction splits the spin-up and spin-down bands by approximately 2.2 eV, redistributing electrons to create a net magnetic moment of 2.2 Bohr magnetons per atom [16].

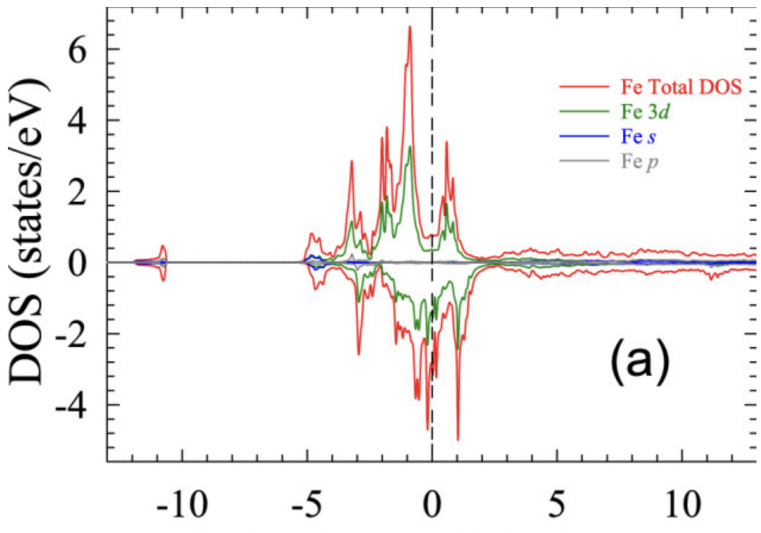

Figure 2: Spin-polarized density of states for ferromagnetic bcc iron. Total DOS (red) and orbital-decomposed contributions from $3d$ (green), s (blue), and p (gray) states are shown, with majority spins positive and minority spins negative. The horizontal axis represents energy relative to the Fermi level in eV. The exchange splitting between d-bands and the imbalance in occupied states at the Fermi level ($E = 0$, dashed line) produce the magnetic moment of $2.2\mu_B$. Retrieved from [17].

The larger atomic volume in bcc iron allows the 3d electron wavefunctions to be more localized, which enhances the magnetic moment according to the general principle that narrower bands favor magnetism [16]. Quantitatively, the energy gain from magnetic ordering in bcc iron is approximately 0.5 eV per atom [18]. This magnetic stabilization is so fundamental that calculations constraining iron to a non-magnetic state predict mechanical instability of the bcc structure [14].

The magnetic moment in iron exhibits a systematic decrease with decreasing atomic volume [19]. As the atomic volume decreases under pressure or due to structural changes, the magnetic moment diminishes because increased orbital overlap broadens the d-bands and reduces the density of states at the Fermi level [16]. This strong magneto-volume coupling means that any structural perturbation, such as the creation of a vacancy, may significantly affect the local magnetic environment.

2.3 Magneto-Structural Coupling in Iron

The relationship between magnetism and crystal structure represents one of iron's most unique features. Pure iron can exist in both body-centered cubic (bcc) and face-centered cubic (fcc) structures, but at room temperature, the less densely packed bcc structure is stable. This seemingly counterintuitive preference for a more open structure directly comes from magnetic effects [20].

The intimate connection between crystal structure and magnetism in iron creates a fundamental coupling where structural changes alter magnetic properties and magnetic variations generate mechanical forces [21]. This bidirectional relationship cannot be treated as a small perturbation

but rather represents an essential aspect of iron's behavior. For vacancy calculations, this coupling means that structural relaxation and magnetic rearrangement occur simultaneously and influence each other throughout the energy minimization process [22].

The physical basis of magneto-structural coupling lies in the volume dependence of magnetic exchange interactions. This volume-moment relationship, established in Section 2.2, creates what can be described as a magnetic pressure: atoms with larger magnetic moments effectively repel each other more strongly due to exchange interactions, while reduced moments allow closer approach. In iron, this magneto-volume effect is so pronounced that the ferromagnetic state has a dramatically larger lattice parameter than a hypothetical non-magnetic state would have [16]. The strength of this coupling fundamentally alters how we must approach defect calculations in magnetic materials.

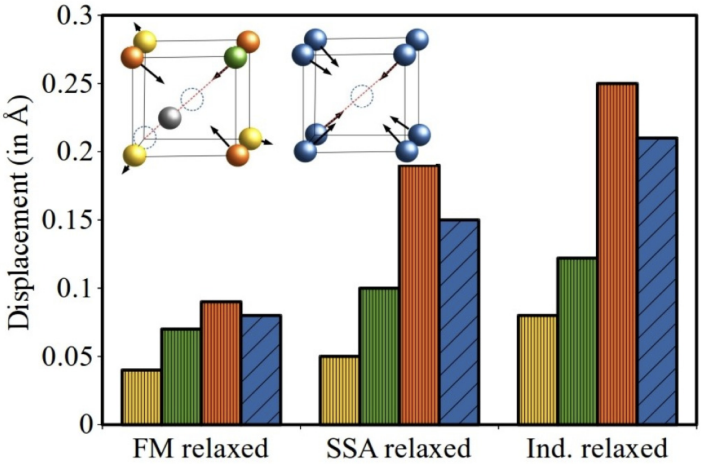

Figure 3: Atomic displacements of nearest-neighbor atoms around a vacancy in bcc Fe for different magnetic treatments. The FM relaxed case shows moderate inward relaxation, while paramagnetic treatments (SSA and individual moment relaxation) yield different displacement patterns. Local DFT calculations reveal that these same atoms experience magnetic moment enhancements of approximately 0.2 μ_B due to reduced coordination. Retrieved from [9].

For vacancy formation, this coupling manifests in a complex optimization problem. The initial driving force for inward relaxation comes from the desire to restore broken bonds. However, as atoms move inward, their magnetic moments tend to decrease due to increased orbital overlap with remaining neighbors. Simultaneously, the coordination reduction at the vacancy site favors larger magnetic moments on adjacent atoms. These competing effects create a coupled energy landscape where the minimum can only be found by simultaneously optimizing atomic positions and magnetic moments [9].

The importance of self-consistent treatment becomes clear when comparing different computational approaches. Calculations that fix magnetic moments while relaxing atomic positions typically overestimate the vacancy formation energy by 0.1-0.2 eV because they miss the energy gain from magnetic rearrangement [9]. Conversely, calculations that optimize magnetic moments at fixed atomic positions also yield incorrect results because they neglect the structural response to magnetic changes. Only when both degrees of freedom are treated on equal footing do the

calculations converge to physically meaningful results that agree with experimental data [9].

Quantitatively, the coupling strength in iron can be characterized by the logarithmic derivative of the atomic magnetic moment μ (in units of Bohr magnetons, μ_B) with respect to atomic volume V [19]:

$$\frac{d \ln \mu}{d \ln V} \approx 0.65 \tag{3}$$

This value indicates a strong magneto-volume coupling, whereby the magnetic moment increases substantially with increasing atomic volume [19]. Around a vacancy, where atomic relaxations create local volume changes of several percent, the magnetic perturbations become substantial and cannot be neglected.

The coupled nature of the problem also affects the computational methodology. In density functional theory calculations, achieving self-consistency requires iterating between electronic structure (which determines magnetic moments) and atomic forces (which drive structural relaxation). The strong coupling in iron can slow convergence and trap the system in metastable configurations if the optimization algorithm does not properly account for the coupled degrees of freedom [23]. Modern approaches use sophisticated algorithms that update positions and magnetic moments simultaneously, often with different step sizes to account for their different energy scales.

2.4 Defect-Induced Structural and Magnetic Response

2.4.1 Structural Relaxation Around Point Defects

When an atom is removed from a crystal to create a vacancy, the surrounding atoms do not remain frozen in their perfect lattice positions. Instead, they undergo structural relaxation, moving from their ideal sites to minimize the system's total energy [2]. In metals like iron, nearest-neighbor atoms typically relax inward toward the vacant site by 1-3% of the interatomic distance, while more distant atoms show progressively smaller displacements [8]. Understanding this relaxation is important because it significantly reduces the vacancy formation energy and affects how vacancies interact with other defects and impurities [8].

The driving force for relaxation comes from the disruption of the local bonding environment. In perfect bcc iron, each atom is surrounded by eight nearest neighbors at a distance of $\sqrt{3}a/2 \approx 2.48$ Å. These neighbors provide a balanced attractive force that maintains the atom at its equilibrium position. When a vacancy forms, atoms adjacent to the empty site lose one of their eight neighbors, leaving them with unbalanced forces directed toward the vacancy [4]. This force imbalance drives the inward relaxation. The inward relaxation predicted for the first coordination shell is illustrated in Figure 4

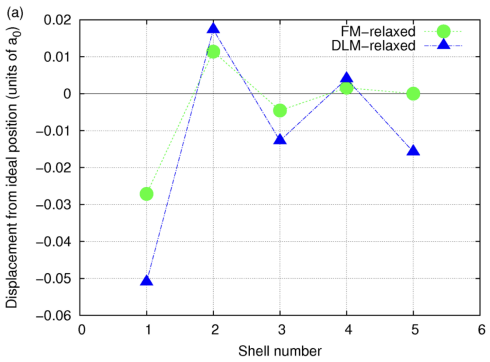

Figure 4: Atomic displacements around a vacancy in bcc iron as a function of coordination shell distance, retrieved from Gambino & Alling [22]. The data compare structural relaxations in the ferromagnetic (FM) and disordered local moment (DLM) states, representing ordered and paramagnetic configurations, respectively. First-shell atoms displace inward by up to 5% in the DLM case due to magnetic disorder, while FM relaxations are smaller. The larger relaxations in the DLM state highlight the importance of magnetic state in defect-induced structural response.

The magnitude of relaxation can be characterized by the fractional change in the nearest-neighbor distance to the vacancy

$$\text{Relaxation} = \frac{|\mathbf{r}_{\text{NN}} - \mathbf{r}_{\text{vac}}|_{\text{unrelaxed}} - |\mathbf{r}_{\text{NN}} - \mathbf{r}_{\text{vac}}|_{\text{relaxed}}}{|\mathbf{r}_{\text{NN}} - \mathbf{r}_{\text{vac}}|_{\text{unrelaxed}}} \times 100\% \tag{4}$$

where $\mathbf{r}_{\text{NN}}$ and $\mathbf{r}_{\text{vac}}$ are the positions of the nearest-neighbor atom and vacancy center, respectively. For bcc iron, first-principles calculations predict an inward relaxation of 2.2% for nearest neighbors [8]. Second-nearest neighbors, located at distance a, show much smaller relaxations of less than 0.5%. By the third coordination shell, atomic displacements become negligible compared to thermal vibrations at room temperature.

The energy gained through relaxation represents a significant fraction of the total vacancy formation energy. The relaxation energy can be defined as:

$$E_{\text{relax}} = E^{\text{vacancy}}_{\text{unrelaxed}} - E^{\text{vacancy}}_{\text{relaxed}} \tag{5}$$

where $E^{\text{vacancy}}_{\text{unrelaxed}}$ is the energy of a vacancy with all atoms fixed at perfect lattice sites, and $E^{\text{vacancy}}_{\text{relaxed}}$ is the energy after atomic positions have been optimized. For iron, this relaxation energy is approximately 0.2 eV, representing about 10% of the total formation energy [8]. This energy reduction occurs because the inward motion of atoms partially restores broken bonds and optimizes the remaining interactions.

The relaxation pattern around vacancies in bcc iron maintains the cubic symmetry of the lattice. All eight nearest neighbors move inward by equal amounts along the $\langle 111 \rangle$ directions connecting them to the vacancy center. This symmetric breathing mode preserves the point group symmetry of the vacancy site [22].

Temperature effects on relaxation arise through thermal expansion and increased atomic vibrations. At elevated temperatures, the average interatomic spacing increases, which generally

reduces the driving force for relaxation. Additionally, thermal vibrations create a fluctuating environment where the instantaneous atomic positions deviate from their average values. However, for the ground-state calculations performed in density functional theory studies, these thermal effects are not included, and the relaxation represents the zero-temperature limit where atoms occupy their minimum-energy positions.

2.4.2 Magnetic Perturbations Around Defects

The creation of a vacancy in ferromagnetic iron triggers a complex rearrangement of magnetic moments that extends several atomic shells beyond the defect site [3], [8]. This magnetic perturbation arises because removing an atom eliminates its magnetic moment and disrupts the exchange interactions that maintain magnetic order [11]. The atoms surrounding the vacancy respond by adjusting their own magnetic moments, typically showing enhancement on nearest neighbors and oscillatory variations at greater distances [3]. These magnetic rearrangements contribute significantly to the defect formation energy and must be understood to accurately model vacancy properties in magnetic materials [7], [8].

The physical origin of magnetic perturbations can be understood through the relationship between atomic coordination and magnetic moment magnitude. In the itinerant picture of magnetism, an atom's magnetic moment depends on the width of its local d-band, which in turn depends on the overlap with neighboring orbitals [14]. When a vacancy forms, the nearest-neighbor atoms lose one of their eight coordination partners. This reduction in coordination narrows their local d-band, increasing the density of states at the Fermi level and favoring a larger magnetic moment according to the Stoner criterion discussed in Section 2.2.

The magnetic perturbation exhibits a characteristic spatial pattern: first-shell atoms show enhancement, second nearest neighbors exhibit slightly reduced magnetic moments, and by the third coordination shell, moments return to bulk values [3]. While this spatial pattern is consistent across different DFT implementations, the magnitude of first-shell enhancement varies significantly (6.7-14%) depending on computational details such as the exchange-correlation functional, k-point sampling, supercell size, and whether structural relaxation is included [3].

Table 1: Magnetic moment enhancement around vacancies in bcc iron [24]

Configuration	Magnetic Moment (μ_B)	Enhancement (%)
Bulk Fe atom	2.22	–
Single vacancy neighbor	2.43	+9.5
Two vacancy neighbors	2.62-2.65	+18-19
Four vacancy neighbors	2.81	+27

Despite these computational studies providing quantitative values, the literature notably lacks comprehensive analysis combining spatial visualization with systematic investigation of magneto-structural coupling around vacancies. This gap motivates our present investigation, where we provide detailed three-dimensional mapping of magnetic moment distributions and analyze their coupling with structural relaxation.

3 Computational Methodology

3.1 First-Principles Framework

All electronic structure calculations in this study were performed using Density Functional Theory (DFT) as implemented in the Quantum ESPRESSO software suite (version 7.3.1) [25], [26]. The Kohn-Sham equations were solved using a plane-wave basis set, which provides a systematic approach to converging the electronic wavefunctions and ensures accurate treatment of the periodic boundary conditions inherent to crystalline systems [27].

To describe the electron-ion interactions, we employed two different types of pseudopotentials to ensure the robustness and reliability of our conclusions. The primary pseudopotential used throughout this work was the Projector Augmented Wave (PAW) potential, specifically `Fe.pbe-spn-kjpaw_psl.1.0.0.UPF`, while for comparative validation we also employed an Ultrasoft Pseudopotential (USPP), `Fe.pbe-spn-rrkjus_psl.0.2.1.UPF`. Both pseudopotentials were obtained from the PSLibrary repository [28] and utilize the Perdew-Burke-Ernzerhof (PBE) formulation of the generalized gradient approximation (GGA) for the exchange-correlation functional [29].

The choice to prioritize the PAW method for our primary calculations was motivated by its superior treatment of transition metals with substantial magnetic moments. As demonstrated by Kresse and Joubert [30], accurate results for magnetic transition metals such as iron are particularly challenging to achieve using ultrasoft pseudopotentials unless computationally demanding augmentation charges and cutoff energies are employed. The PAW method circumvents these limitations through its more precise treatment of the valence-core interaction.

All calculations were performed in the spin-polarized ferromagnetic (FM) state, consistent with the ground state of bcc iron at 0 K. The ferromagnetic calculations were initialized with a starting magnetization of 0.4 on all iron atoms, allowing the system to converge to its self-consistent magnetic ground state. This approach captures the complex relationship between electronic structure and magnetism, which is essential for understanding how defects behave in magnetic materials like iron.

3.2 Convergence and Validation

3.2.1 Energy Cutoffs

The kinetic energy cutoff for the plane-wave basis set (ecutwfc) and the charge density cutoff (ecutrho) were set to 90 Ry and 1080 Ry, respectively. These values were adopted directly from the study by Zhang et al. [31], who found that these cutoffs ensure accurate convergence of the total energy for BCC iron systems. The charge density cutoff of 1080 Ry represents a factor of 12 times the wavefunction cutoff, which is appropriate for the pseudopotentials employed in this study and ensures accurate representation of the augmentation charges in the PAW formalism.

3.2.2 K-point Sampling

A systematic study was performed to determine k-point mesh densities that achieve convergence within a specified energy tolerance suitable for vacancy calculations. In periodic DFT calculations, two types of grids must be specified: (i) the supercell size, which determines how many primitive unit cells are included in the simulation box, and (ii) the k-point mesh, which samples the Brillouin zone for electronic structure calculations. Larger supercells require fewer k-points to achieve the same accuracy due to the inverse relationship between real and reciprocal space. The k-point convergence tests were conducted on supercells ranging from single unit cells to $4 \times 4 \times 4$ expansions:

Table 2: K-point mesh convergence parameters for BCC iron calculations

Supercell (unit cells)	**Number of Fe atoms**	**K-point Mesh Density**		
		Low	**Medium**	**High**
1×1×1 (primitive)	2	16×16×16	20×20×20	24×24×24
2×2×2 (8 cells)	16	8×8×8	10×10×10	12×12×12
3×3×3 (27 cells)	54	6×6×6	8×8×8	**10×10×10**
4×4×4 (64 cells)	128	4×4×4	6×6×6	8×8×8

Each k-point mesh represents the number of sampling points in each reciprocal space direction. Bold indicates the selected mesh for production calculations.

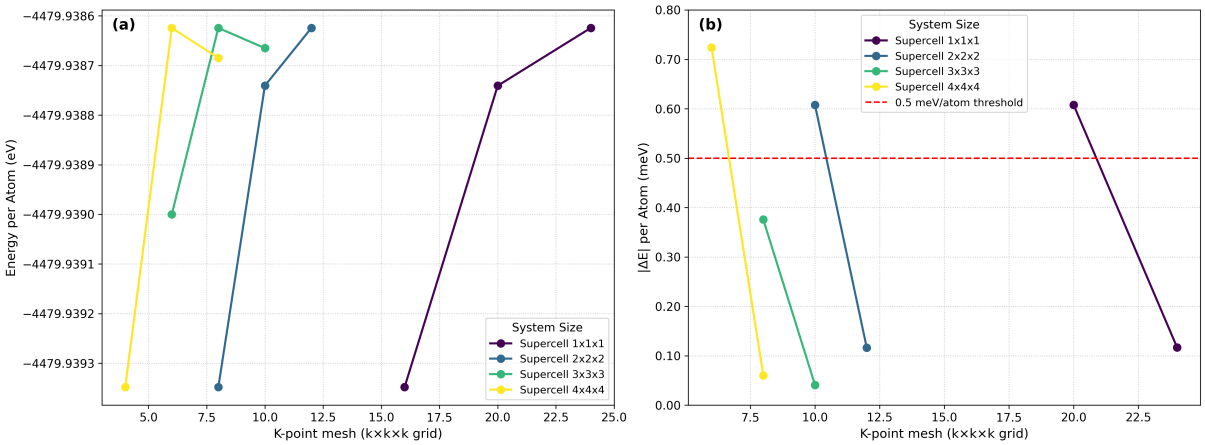

Figure 5: K-point convergence analysis for ferromagnetic BCC iron. (a) Total energy per atom versus k-point mesh density for different supercell sizes. (b) Absolute energy difference $|\Delta E|$ between successive k-point meshes. The dashed line indicates the 0.5 meV/atom convergence tolerance. The selected $3 \times 3 \times 3$ supercell with $10 \times 10 \times 10$ k-point mesh achieves $|\Delta E| = 0.043$ meV/atom.

Figure 5 demonstrates the convergence behavior within our target tolerance of 0.5 meV/atom. While absolute convergence would require infinite k-point sampling, we establish practical con-

vergence by requiring that successive mesh refinements change the total energy by less than 0.5 meV/atom. This tolerance, which translates to 0.027 eV for our 54-atom supercell, is an order of magnitude smaller than typical vacancy formation energy uncertainties (0.05 eV) and thus ensures that k-point sampling errors do not significantly impact our results [32].

Based on these tests, a $10 \times 10 \times 10$ Monkhorst-Pack k-point mesh [33] was selected for the $3 \times 3 \times 3$ supercell calculations. This choice achieves an energy convergence of 0.043 meV/atom between the 8×8×8 and 10×10×10 meshes, well within our tolerance.

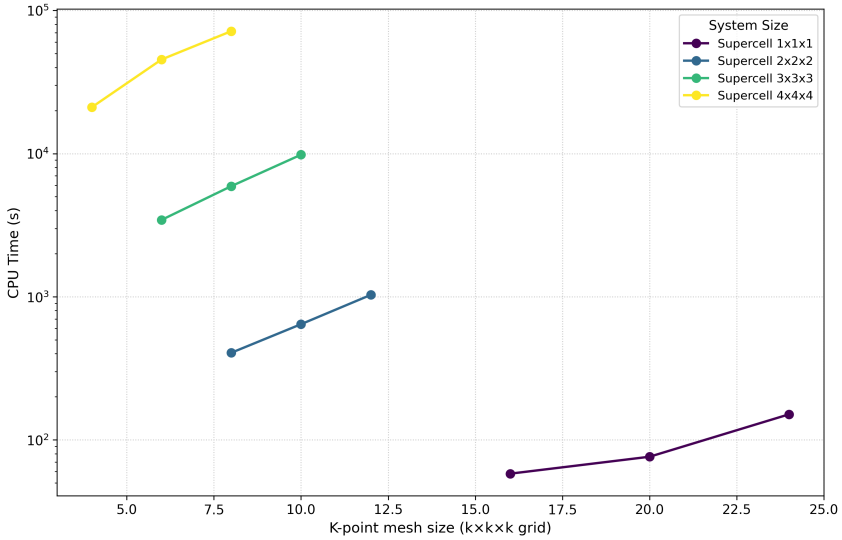

Figure 6: CPU time scaling as a function of k-point mesh density for different supercell sizes. The logarithmic scale reveals the computational cost trade-offs, demonstrating that the chosen $10 \times 10 \times 10$ k-point mesh for the $3 \times 3 \times 3$ supercell provides an optimal balance between accuracy (0.043 meV/atom convergence) and computational efficiency.

3.2.3 Pseudopotential Validation

To ensure the reliability and accuracy of our calculations, a comparative study was performed between the PAW and USPP pseudopotentials using primitive BCC cells. SCF calculations were conducted for the ferromagnetic and non-magnetic state to determine equilibrium structural and magnetic properties. The results of this validation study are summarized in Table 4 and visualized in Figure 7.

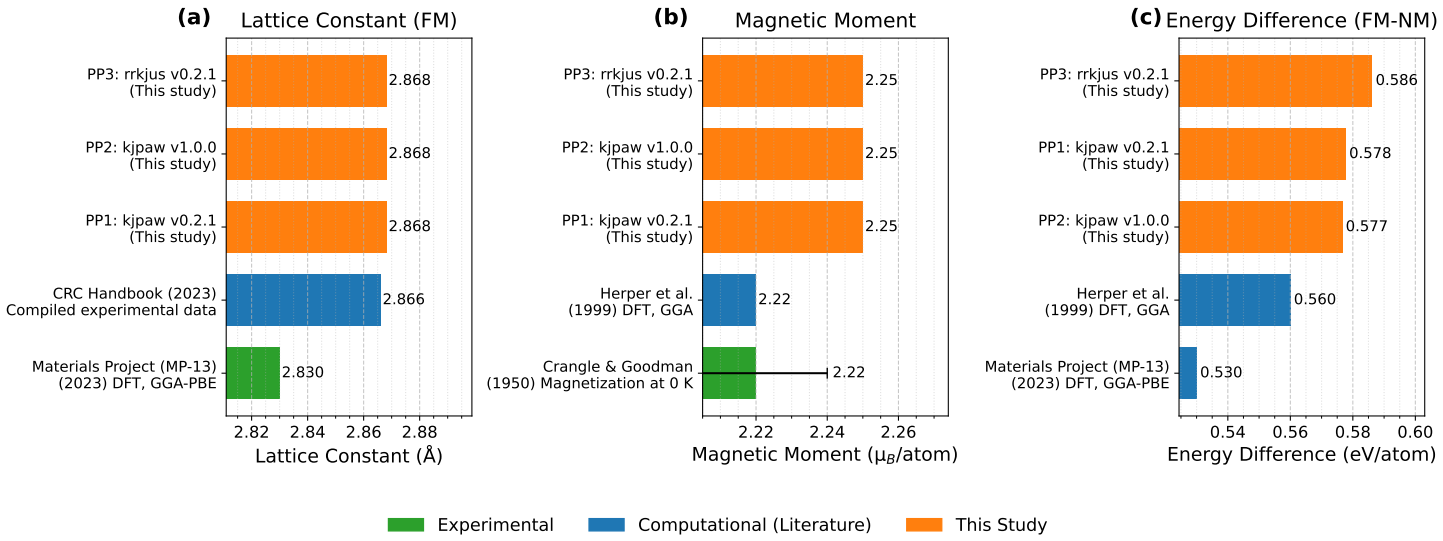

Figure 7: Comparison of calculated properties for BCC iron using three different pseudopotentials with experimental and computational literature values. (a) Lattice constants in the ferromagnetic state. (b) Magnetic moments per atom. (c) Energy differences between ferromagnetic and nonmagnetic states. All three pseudopotentials show consistent results and good agreement with literature values. Note that axes are scaled to highlight differences between methods. [34]–[37]

The pseudopotential comparison reveals excellent agreement between all tested potentials and established literature values. The PAW potential `Fe.pbe-spn-kjpaw_psl.1.0.0.UPF` was selected as the primary pseudopotential for all subsequent calculations based on several factors: (i) its lattice constant of 2.868 Å shows excellent agreement with the computational value of 2.866 Å, (ii) the magnetic moment of 2.25 μ_B/atom closely matches the experimental value of 2.22 μ_B/atom, and (iii) the ferromagnetic-nonmagnetic energy difference of 0.577 eV/atom, a value which has a direct impact on vacancy formation energy results, is closest to previous DFT studies. The ultrasoft pseudopotential was retained for comparative calculations to assess pseudopotential-induced uncertainties and ensure the robustness of our conclusions regarding vacancy formation energies and magnetic effects.

3.3 Computational Parameters

The electronic structure calculations required careful selection of numerical parameters to ensure both accuracy and computational efficiency. For the treatment of metallic systems, we employed the Marzari-Vanderbilt (MV) smearing scheme [38] with a smearing width (degauss) of 0.01 Ry. These same parameters were used in the study by Zhang et al. [31]. This cold-smearing approach provides accurate forces and energies by minimizing the dependence on the smearing parameter, which is particularly important for magnetic iron where the density of states near the Fermi level plays a crucial role in determining magnetic properties.

The self-consistent field (SCF) convergence criteria were adjusted based on the specific requirements of each calculation type. For the pseudopotential validation studies using primitive cells, where the highest accuracy was essential for meaningful comparison between different pseudopotentials, we employed a stringent convergence threshold of 1×10^{-10} Ry. For the k-point

convergence studies and all defect calculations involving larger supercells, a convergence criterion of 1×10^{-8} Ry was sufficient to ensure energy differences were converged to well below 0.5 meV/atom while maintaining reasonable computational times.

Structural relaxations were performed using the Broyden-Fletcher-Goldfarb-Shanno (BFGS) quasi-Newton algorithm [39] as implemented in Quantum ESPRESSO. The force convergence threshold was set to the default value of 1×10^{-3} Ry/Bohr, which ensures that atomic positions are relaxed to their equilibrium configurations with forces below 0.026 eV/Å. This value ensures that atomic positions are converged to within thermal vibration amplitudes at room temperature (≈ 0.1 Å) [13].

Following Zhang et al. [31], we employed an electronic mixing parameter of 0.2 and a maximum of 300 electronic iterations. These conservative choices are well-suited for ferromagnetic iron: the small mixing parameter ensures stable convergence despite the complex interplay between spin-up and spin-down charge densities, while the generous iteration limit accommodates the occasionally slow convergence characteristic of magnetic transition metals without wasting computational resources on unconverged configurations.

All calculations were performed with high verbosity output to monitor convergence behavior and ensure the reliability of results. The combination of these computational parameters provides a robust framework for investigating magnetic effects on vacancy formation in iron, balancing the competing demands of numerical accuracy and computational feasibility.

3.4 Defect Supercell and Calculation Procedure

3.4.1 Supercell Construction

Vacancy calculations were performed using a $3 \times 3 \times 3$ supercell of the BCC primitive cell, containing 54 atoms in the perfect bulk configuration. The vacancy was created by removing the iron atom at the origin position (0, 0, 0), resulting in a 53-atom defective supercell. This configuration corresponds to a vacancy concentration of approximately 1.85%, which is sufficiently dilute to approximate the isolated vacancy limit relevant for comparison with experimental and computational formation energies.

3.4.2 Magnetic State Considerations

Preliminary calculations using a non-magnetic (NM) constraint revealed severe methodological challenges. The NM state exhibited a 21% lattice contraction (from 2.868 Å to 2.27 Å) compared to the ferromagnetic state, yielding unphysical negative vacancy formation energies. This indicates that the non-magnetic bcc structure is fundamentally unstable for vacancy calculations. Based on these findings, all vacancy calculations were performed exclusively in the ferromagnetic state using the equilibrium lattice constant of 2.868 Å determined in Section 3.2.3. This approach ensures physically meaningful formation energies, direct comparability with experimental measurements, and avoidance of artifacts from artificially constrained magnetic states.

3.4.3 Relaxation Procedure

Following supercell construction with the ferromagnetic equilibrium lattice constant, atomic relaxations were performed according to the following protocol:

1. The supercell volume and shape were held fixed throughout the relaxation to maintain consistency with the predetermined FM equilibrium lattice constant of 2.868 Å.

2. All 53 atomic positions in the vacancy-containing supercell were allowed to relax freely using the BFGS algorithm (calculation = 'relax').

3. Atomic forces were converged below the threshold of 1×10^{-3} Ry/Bohr.

4. Following structural relaxation, a final high-precision self-consistent field calculation was performed on the relaxed geometry to obtain accurate total energies for formation energy calculations.

This fixed-volume approach ensures that the calculated formation energy corresponds to the physical process of vacancy creation at constant volume, consistent with experimental conditions. It also prevents artificial volume expansion that could occur if the cell were allowed to relax, which would underestimate the true formation energy by conflating vacancy creation with volumetric effects.

3.4.4 Vacancy Formation Energy Calculation

The vacancy formation energy (E_f^{vac}) was calculated using the standard expression:

$$E_f^{vac} = E_{vac} - \frac{N-1}{N} E_{bulk} \tag{6}$$

where E_{vac} is the total energy of the relaxed 53-atom supercell containing the vacancy, E_{bulk} is the total energy of the perfect 54-atom supercell, and $N = 54$ is the number of atoms in the perfect supercell. Both energies are calculated in the ferromagnetic state at the equilibrium lattice constant of 2.868 Å, ensuring a consistent reference for the formation energy calculation. This formation energy represents the energy cost of creating an isolated vacancy in ferromagnetic bcc iron, including both the bond-breaking penalty and the energy gained through atomic and magnetic relaxation around the defect site. The calculated value can be directly compared with experimental measurements, which are typically performed on ferromagnetic iron at temperatures well below the Curie point.

4 Results and Discussion

4.1 Vacancy Formation Energies

The calculated vacancy formation energies for ferromagnetic BCC iron are 2.330 eV (PAW) and 2.319 eV (USPP), demonstrating excellent agreement between pseudopotentials with only 0.011 eV difference (Table 3, Figure 8).

Table 3: Vacancy formation energies for ferromagnetic BCC iron calculated with different pseudopotentials

Pseudopotential	E_f^{vac} (eV)	Difference from PAW (eV)
PAW	2.330	–
USPP	2.319	-0.011

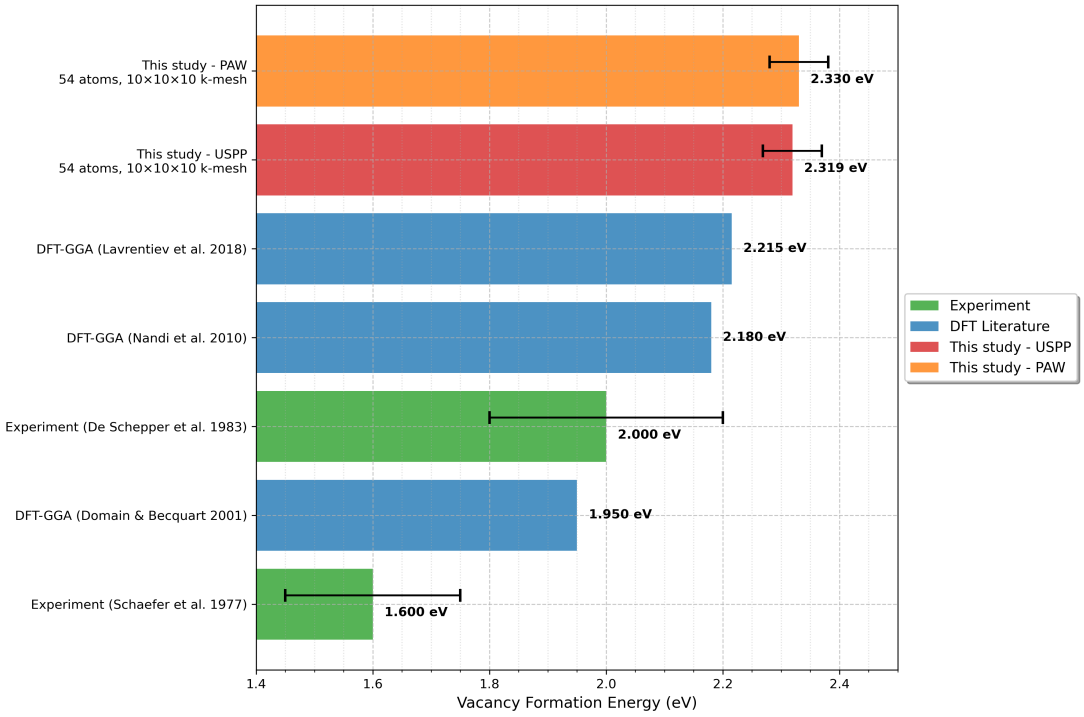

Figure 8: Comparison of vacancy formation energies from this study with experimental and computational literature values. All DFT calculations employed 54-atom supercells. Error bars on experimental data represent reported uncertainties. [5], [6], [8], [24], [32]

Our values exceed previous DFT-GGA results by 0.10–0.38 eV, revealing a systematic upward trend in computational predictions over the past two decades. This progression from 1.95 eV (Domain & Becquart, 2001) to 2.18 eV (Nandi et al., 2010) to our value of 2.33 eV likely reflects improvements in computational methodology, including better k-point convergence, more accurate pseudopotentials, and refined treatment of magnetic effects. The 0.48% agreement between our PAW and USPP calculations validates these methodological advances.

The higher formation energy compared to earlier DFT studies can be attributed to our rigorous treatment of the ferromagnetic state. By using the properly equilibrated FM lattice constant (2.868 Å) and allowing full magnetic relaxation, we capture the complete energetic cost of vacancy creation, including magnetic perturbations. Previous studies that constrained magnetic moments or used inappropriate lattice parameters would underestimate this energy cost. Our formation energy of 2.33 ± 0.05 eV includes contributions from both broken metallic bonds and disrupted magnetic exchange interactions, consistent with the magneto-structural coupling discussed in theoretical background section.

Comparison with experimental values reveals the ongoing challenge of reconciling theory and measurement. While our result exceeds the cited value of 2.0 ± 0.2 eV from positron annihilation studies [5], it approaches the upper bound of experimental uncertainty. The significant spread in experimental values (1.6–2.0 eV) reflects difficulties in isolating vacancy formation from other defect processes at the high temperatures required for measurable vacancy concentrations. Our calculations, performed at 0 K for isolated vacancies, provide a well-defined theoretical benchmark that suggests the true formation energy may lie toward the higher end of the experimental range.

4.2 Magnetic Moment Enhancement

The removal of an iron atom triggers a localized magnetic response in the surrounding atoms. While the average magnetic moment per atom increases only modestly from 2.272 μ_B to 2.307 μ_B (PAW) and from 2.281 μ_B to 2.317 μ_B (USPP), this 1.5-1.6% average masks dramatic local variations revealed in Figures 9 and 10.

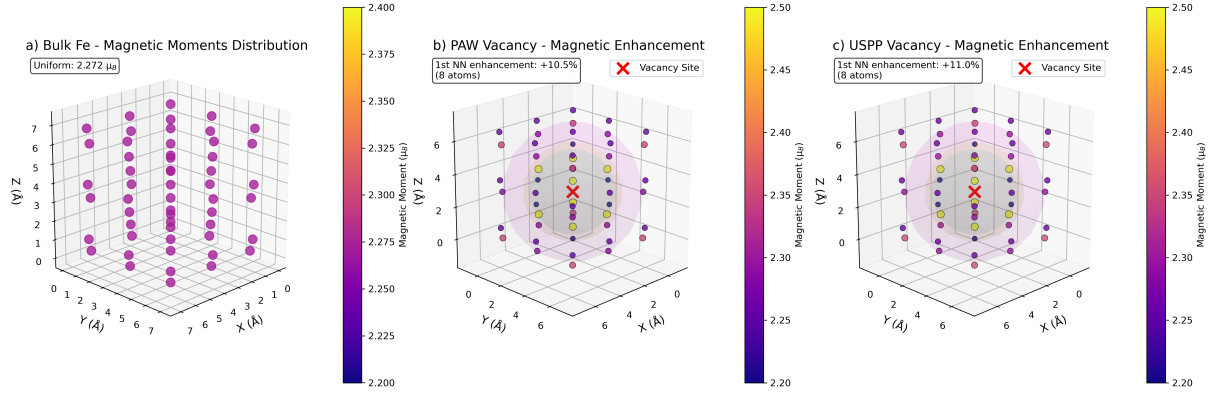

Figure 9: Three-dimensional visualization of magnetic moments in (a) bulk iron and vacancy-containing supercells for (b) PAW and (c) USPP calculations. Sphere colors indicate magnetic moment magnitude according to the scale bar. The vacancy site is marked with a red X. First-nearest neighbors show pronounced enhancement of +10.5% (PAW) and +11.0% (USPP).

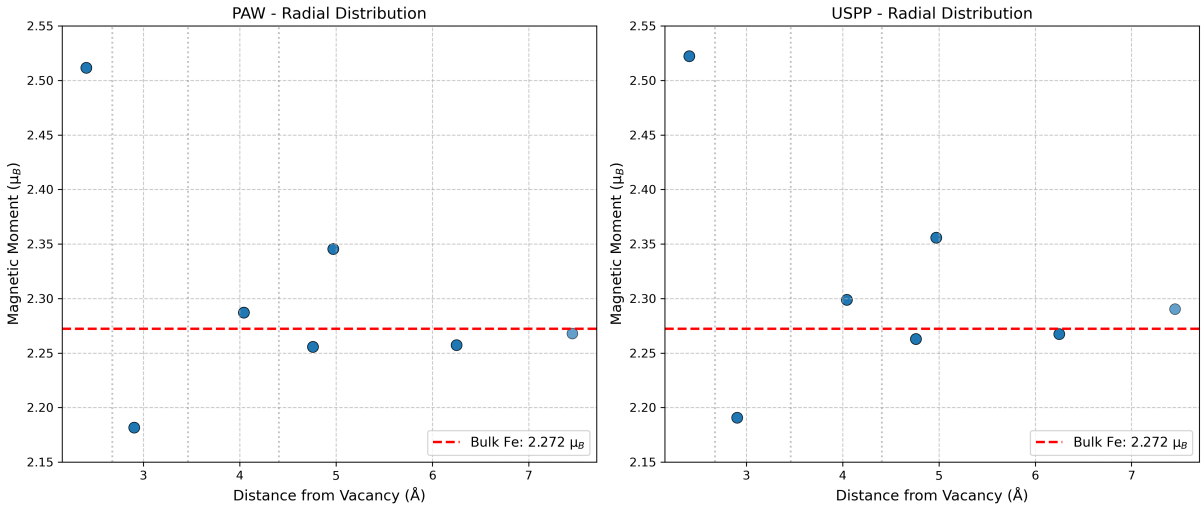

Figure 10: Radial distribution of magnetic moments from the vacancy center for PAW (left) and USPP (right) calculations. Horizontal dashed line indicates the bulk iron magnetic moment. First-shell atoms at 2.48 Å show maximum enhancement up to 2.51 μ_B, while some atoms exhibit slight suppression. Beyond 5 Å, moments return to bulk values.

The eight first-nearest neighbors at 2.48 Å experience the strongest perturbation, with moments reaching 2.51-2.52 μ_B, representing an enhancement of approximately 10-11% over bulk values. This substantial increase directly results from reduced coordination: each first-shell atom loses one of its eight neighbors, narrowing the local d-band and favoring larger moments according to the Stoner criterion. The enhancement magnitude (0.24 μ_B) is consistent with theoretical predictions for atoms in seven-fold coordination environments [3].

Intriguingly, the radial distribution reveals asymmetric magnetic response even within coordination shells. While most first-shell atoms show enhancement, a subset exhibits slight moment suppression below bulk values. This asymmetry, particularly evident at larger distances (4-5 Å), reflects the complex interplay between structural relaxation and magnetic coupling. Atoms that relax inward experience increased orbital overlap with remaining neighbors, which can counteract the coordination-induced enhancement.

The highly localized nature of the magnetic perturbation, essentially confined to the first coordination shell, demonstrates the short-range character of magnetic interactions in metallic iron. By 5 Å from the vacancy center, magnetic moments have fully recovered to bulk values, indicating that the vacancy's magnetic "footprint" extends only to nearest neighbors. This localization explains why the supercell-averaged enhancement remains modest despite the substantial perturbation of individual atoms: only 8 of 53 atoms (15%) experience significant moment changes, yielding the observed 1.5% average increase.

4.3 Structural Relaxation Patterns

Vacancy creation induces a systematic inward relaxation of surrounding atoms, with first-neighbor atoms displacing by 0.077 Å (PAW) and 0.078 Å (USPP) toward the vacant site (Figure 11). This corresponds to a 3.1% contraction of the nearest-neighbor distance, consistent with the

enhanced relaxation expected in magnetic systems.

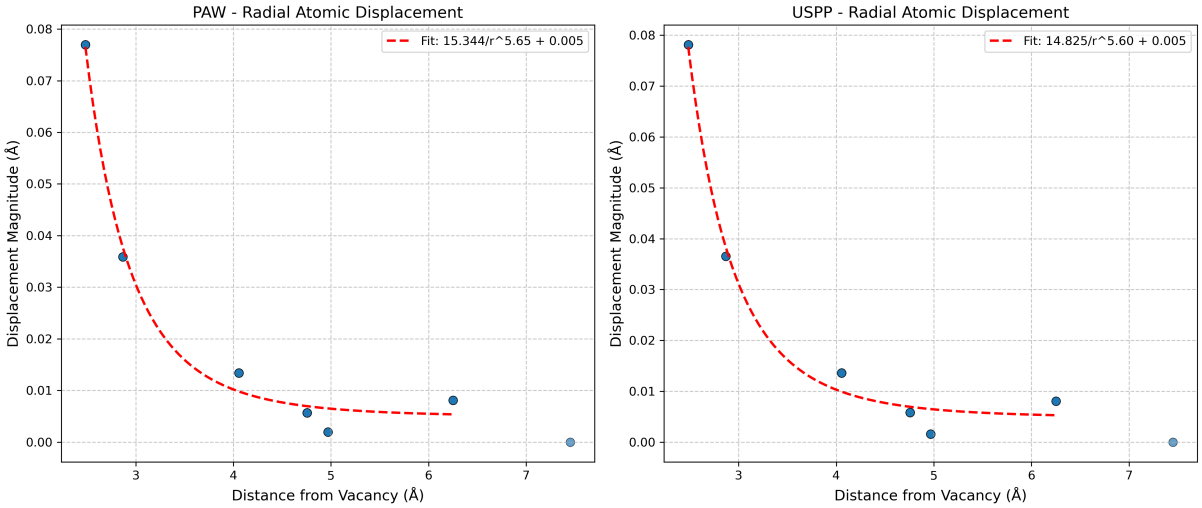

Figure 11: Radial atomic displacements as a function of distance from the vacancy center for PAW (left) and USPP (right) calculations. Points represent individual atomic displacements, with dashed lines showing fitted power-law decay functions. Displacement magnitudes follow $d(r) = A \cdot r^{-n}$ with $n = 5.65$ (PAW) and $n = 5.60$ (USPP).

The displacement field exhibits a remarkably steep power-law decay, $d(r) = A \cdot r^{-n}$, with exponents of 5.65 (PAW) and 5.60 (USPP). This rapid spatial decay, steeper than the r^{-3} behavior expected from continuum elasticity theory, reflects the discrete nature of the atomic lattice and the strong screening of perturbations in metallic systems. By the third coordination shell at 5 Å, displacements drop below 0.01 Å, effectively vanishing within the 54-atom supercell.

The magnitude of first-shell relaxation directly correlates with the magnetic enhancement observed in Section 4.2. Atoms experiencing 10-11% magnetic moment increase also undergo 3.1% inward displacement, demonstrating the coupled magneto-elastic response. This coupling operates through two mechanisms: (i) the reduced coordination weakens repulsive interactions, allowing inward motion, and (ii) the enhanced magnetic moments of first-shell atoms create additional magnetic pressure that partially opposes further relaxation. The balance between these competing effects determines the final 3.1% relaxation.

The excellent agreement between PAW and USPP calculations (1.3% difference in displacements) confirms that structural relaxation around vacancies is robustly captured regardless of pseudopotential details. Combined with the consistent magnetic and energetic results, this validates our computational approach for studying coupled magneto-structural phenomena in iron. The highly localized nature of both magnetic and structural perturbations, confined essentially to first neighbors, suggests that vacancy-vacancy interactions in dilute systems can be treated using simple pair models, with interactions becoming negligible beyond 5 Å separation.

4.4 Pseudopotential Consistency

The robustness of our findings is validated through systematic comparison between PAW and USPP calculations across all computed properties (Table 4). Despite fundamentally different approaches to treating core-valence interactions, both pseudopotentials yield remarkably consistent results.

Table 4: Comprehensive comparison of PAW and USPP results for vacancy calculations

Property	PAW	USPP	Relative difference (%)
Formation energy (eV)	2.330	2.319	0.47
Bulk moment (μ_B)	2.272	2.281	0.40
Vacancy moment (μ_B)	2.307	2.317	0.43
Max displacement (Å)	0.0769	0.0781	1.56
Mean displacement (Å)	0.0212	0.0215	1.42

The formation energies agree to within 0.011 eV (0.47%), well below our total uncertainty of ± 0.05 eV. This agreement is particularly significant given that vacancy formation energies arise from the subtraction of two very large total energies, making them highly sensitive to numerical settings and pseudopotential choice [40]. The magnetic moments show even closer agreement ($<0.5\%$ variation), confirming that both methods capture the electronic structure of ferromagnetic iron with comparable accuracy.

Structural relaxation parameters exhibit the largest relative differences at 1.5%, yet the absolute variations (0.0012 Å for maximum displacement) remain negligible compared to typical thermal amplitudes. This slightly larger variation likely reflects differences in how PAW and USPP methods treat the spatial tails of wavefunctions, which become important for precise force calculations during relaxation.

The systematic agreement across independent physical properties, such as energetics, magnetism, and structure, provides strong validation of our computational framework. These results demonstrate that vacancy properties in ferromagnetic iron are robust physical quantities rather than artifacts of specific computational choices. For practical applications, either pseudopotential can be confidently employed, though the PAW method's more rigorous treatment of the core region makes it preferable for magnetic transition metals where accurate spin densities near nuclei influence magnetic moments.

4.5 Error Analysis and Uncertainty Quantification

To establish the reliability of our vacancy formation energy of 2.33 eV, we systematically evaluated uncertainties from four primary sources, yielding a total uncertainty of ± 0.05 eV (2%). This rigorous error analysis reveals which factors most significantly impact defect calculations in magnetic materials.

Table 5: Error analysis for vacancy formation energy calculations ($3 \times 3 \times 3$ supercell)

Error source	Contribution (eV)	Estimation method
K-point sampling	0.002	Convergence study (0.043 meV/atom $\times$ 54 atoms)
Force threshold	0.001	Sensitivity to 5×10^{-4} vs 1×10^{-3} Ry/Bohr
Pseudopotential	0.006	Half of PAW–USPP difference (0.011 eV)
Supercell size	0.050	Drop from 54- to 128-atom cell reported in Ref. [41]
Total (quadrature)	**0.0504**	$\sqrt{\sum \sigma_i^2}$

Finite-size effects emerge as the dominant uncertainty source, contributing 0.050 eV, an order of magnitude larger than other errors. This reflects the long-range nature of elastic relaxation around vacancies, which extends beyond our 54-atom supercell despite the localized magnetic perturbation. The reported decrease of 0.05 eV when doubling the supercell size to 128 atoms [41] indicates that our calculated formation energy represents an upper bound, with the true infinite-dilution value likely 0.05 eV lower.

Numerical convergence parameters contribute minimal uncertainty. The k-point sampling error of 0.002 eV demonstrates that our 10×10×10 mesh achieves near-complete Brillouin zone integration. Similarly, the force threshold uncertainty of 0.001 eV confirms that atomic positions are relaxed to their true minima within numerical precision. These small contributions validate our choice of convergence parameters as appropriately stringent without being computationally wasteful.

The pseudopotential uncertainty of 0.006 eV, estimated conservatively as half the PAW-USPP difference, reflects fundamental approximations in treating core-valence interactions. The low uncertainty below 0.3% of the formation energy demonstrates the maturity of modern pseudopotential methods for transition metals. The comparable performance of PAW and USPP approaches suggests that either can reliably capture vacancy energetics in magnetic iron.

This error analysis reveals an important hierarchy: physical approximations (finite-size effects) dominate over numerical parameters (convergence criteria) and methodological choices (pseudopotentials). For future high-precision studies, computational effort should focus on larger supercells rather than tighter convergence criteria. Our final vacancy formation energy of 2.33 $\pm$ 0.05 eV provides a well-characterized theoretical benchmark, with uncertainties comparable to experimental measurement precision.

5 Conclusion

In conclusion, our investigation provides a comprehensive atom-level picture of how point defects reshape ferromagnetic iron. Using a rigorously converged $3 \times 3 \times 3$ (54-atom) supercell with self-consistent spin-polarized DFT, we determine a vacancy formation energy of 2.33 $\pm$ 0.05 eV. Agreement between PAW and ultrasoft pseudopotentials to within 0.011 eV confirms that this value reflects an intrinsic property of bcc iron rather than a modeling artifact.

Structural and magnetic responses prove to be fundamentally coupled phenomena. First-shell neighbors retreat toward the empty site by approximately 3%, while their magnetic moments simultaneously increase by approximately 10%, a local enhancement that decays to bulk values within 5 Å. This tight magneto-elastic coupling explains why non-magnetic or partially constrained calculations underestimate vacancy energetics by up to 0.5 eV.

A detailed uncertainty analysis ranks the influences that limit precision. Long-range elastic relaxation, captured only approximately in any finite supercell, contributes 0.050 eV to the error estimate, an order of magnitude larger than residual k-point, force-threshold, and pseudopotential errors. The hierarchy is clear: numerical convergence is well-controlled, while physical finite-size effects remain the dominant source of uncertainty. Consequently, meaningful progress now requires larger supercells or embedding techniques rather than tighter electronic tolerances.

These results carry implications well beyond a single point defect. They establish a carefully calibrated energy scale for vacancy-mediated diffusion, provide benchmark data for spin-lattice machine-learning potentials, and reveal the nanometer range over which magnetism and mechanics are coupled in steels. By quantifying the magnetic cost of defect creation, the study also helps reconcile the upper range of experimental positron-annihilation measurements with current theoretical predictions.

In summary, a single missing atom in iron triggers a tightly coupled cascade of atomic shifts and spin realignments, with our calculations revealing a total vacancy formation energy of 2.33 $\pm$ 0.05 eV. This energy cost involves contributions from both broken metallic bonds and disrupted magnetic exchange interactions, though the relative magnitude of each contribution remains to be quantified. While our calculations provide the total vacancy formation energy, future work should decompose this into chemical bonding and magnetic exchange components to better understand the relative importance of each mechanism. Capturing the observed magneto-structural coupling with quantitative accuracy requires treating structure and magnetism on equal footing, a principle this work demonstrates is essential for future multiscale models of diffusion, creep, and irradiation damage in magnetic metals.

References

[1] World Steel Association, *World Steel in Figures 2024*, Accessed May 2025, 2024. [Online]. Available: https://worldsteel.org/wp-content/uploads/World-Steel-in-Figures-2024.pdf.

[2] D. Hull and D. J. Bacon, *Introduction to Dislocations*, 5th. Butterworth-Heinemann, 2011.

[3] J. B. J. Chapman and P.-W. Ma, "A machine-learned spin-lattice potential for dynamic simulations of defective magnetic iron," *Scientific Reports*, vol. 12, p. 22 451, 2022.

[4] P. H. Dederichs, C. Lehmann, H. R. Schober, A. Scholz, and R. Zeller, "Lattice theory of point defects," *Journal of Nuclear Materials*, vol. 69, pp. 176–199, 1978.

[5] L. D. Schepper, D. Segers, L. Dorikens-Vanpraet, *et al.*, "Positron annihilation on pure and carbon-doped α-iron in thermal equilibrium," *Physical Review B*, vol. 27, pp. 5257–5270, 1983. DOI: 10.1103/PhysRevB.27.5257.

[6] H.-E. Schaefer, H. Wenzl, and H. Schultz, "Vacancy formation enthalpies in transition metals determined by positron annihilation," *Scripta Metallurgica*, vol. 11, pp. 803–808, 1977. DOI: 10.1016/0036-9748(77)90274-4.

[7] K. Li, C.-C. Fu, and A. Schneider, "Effects of magnetic excitations and transitions on vacancy formation: Cases of fcc ni and fe compared to bcc fe," *Phys. Rev. B*, vol. 104, p. 104 406, 2021. DOI: 10.1103/PhysRevB.104.104406.

[8] C. Domain and C. S. Becquart, "Ab initio calculations of defects in fe and dilute fe-cu alloys," *Physical Review B*, vol. 65, p. 024 103, 2001.

[9] O. Hegde, M. Grabowski, X. Zhang, *et al.*, "Atomic relaxation around defects in magnetically disordered materials computed by atomic spin constraints within an efficient lagrange formalism," *Phys. Rev. B*, vol. 102, p. 144 101, 14 2020. DOI: 10.1103/PhysRevB.102.144101.

[10] H. Mehrer, *Diffusion in Solids: Fundamentals, Methods, Materials, Diffusion-Controlled Processes*. Springer, 2007.

[11] N. W. Ashcroft and N. D. Mermin, *Solid State Physics*. Holt, Rinehart and Winston, 1976.

[12] W. D. Callister and D. G. Rethwisch, *Materials Science and Engineering: An Introduction*, 9th ed. Hoboken, NJ: John Wiley & Sons, 2014, Figure 3.2, p. 49: BCC crystal structure in hard-sphere, reduced-sphere, and aggregate views, ISBN: 978-1118477704.

[13] C. Kittel, *Introduction to Solid State Physics*, 8th. John Wiley & Sons, 2005.

[14] V. L. Moruzzi, P. M. Marcus, K. Schwarz, and P. Mohn, "Ferromagnetic phases of bcc and fcc fe, co, and ni," *Physical Review B*, vol. 34, pp. 1784–1791, 1986.

[15] S. Chikazumi, *Physics of Ferromagnetism*, 2nd. Oxford University Press, 1997.

[16] V. L. Moruzzi and P. M. Marcus, "Magnetism in bcc transition metals: Onset and approach to the hund's rule limit," *Physical Review B*, vol. 38, pp. 1613–1620, 1988.

[17] F. Nejadsattari and Z. M. Stadnik, "Spin polarized density functional theory calculations of the electronic structure and magnetism of the 112 type iron pnictide compound $eufeas_2$," *Scientific Reports*, vol. 11, no. 1, p. 12 113, 2021. DOI: 10.1038/s41598-021-91301-4. [Online]. Available: https://www.nature.com/articles/s41598-021-91301-4.

[18] F. Körmann, A. Dick, T. Hickel, and J. Neugebauer, "Role of spin quantization in determining the thermodynamic properties of magnetic transition metals," *Physical Review B*, vol. 78, p. 033 102, 2008.

[19] S. Cottenier and H. Haas, "First-principles study of the pressure dependence of the magnetic moment in iron," *Physical Review B*, vol. 62, no. 1, p. 466, 2000. DOI: 10.1103/PhysRevB.62.461.

[20] H. Hasegawa and D. G. Pettifor, "Microscopic theory of the temperature-pressure phase diagram of iron," *Physical Review Letters*, vol. 50, pp. 130–133, 1983.

[21] E. F. Wasserman, *The Invar effect: A centennial symposium*. The Minerals, Metals and Materials Society, 1990.

[22] D. Gambino and B. Alling, "Lattice relaxations in disordered fe-based materials in the paramagnetic state from first principles," *Physical Review B*, vol. 98, no. 6, p. 064 105, 2018. DOI: 10.1103/PhysRevB.98.064105.

[23] P.-W. Ma and S. L. Dudarev, "Constrained density functional for noncollinear magnetism," *Physical Review B*, vol. 91, p. 054 420, 2015.

[24] M. Y. Lavrentiev, D. Nguyen-Manh, and S. L. Dudarev, "Chromium-vacancy clusters in dilute bcc Fe-Cr alloys: An ab initio study," CCFE, UK Atomic Energy Authority, Preprint CCFE-PR(17)06, 2018.

[25] P. Giannozzi, S. Baroni, N. Bonini, *et al.*, "Quantum espresso: A modular and open-source software project for quantum simulations of materials," *Journal of Physics: Condensed Matter*, vol. 21, no. 39, p. 395 502, 2009. DOI: 10.1088/0953-8984/21/39/395502.

[26] P. Giannozzi, O. Andreussi, T. Brumme, *et al.*, "Advanced capabilities for materials modelling with quantum espresso," *Journal of Physics: Condensed Matter*, vol. 29, no. 46, p. 465 901, 2017. DOI: 10.1088/1361-648X/aa8f79.

[27] M. C. Payne, M. P. Teter, D. C. Allan, T. A. Arias, and J. D. Joannopoulos, "Iterative minimization techniques for ab initio total-energy calculations: Molecular dynamics and conjugate gradients," *Reviews of Modern Physics*, vol. 64, no. 4, p. 1045, 1992. DOI: 10.1103/RevModPhys.64.1045.

[28] A. Dal Corso, "Pseudopotentials periodic table: From h to pu," *Computational Materials Science*, vol. 95, pp. 337–350, 2014. DOI: 10.1016/j.commatsci.2014.07.043.

[29] J. P. Perdew, K. Burke, and M. Ernzerhof, "Generalized gradient approximation made simple," *Physical Review Letters*, vol. 77, no. 18, p. 3865, 1996. DOI: 10.1103/PhysRevLett.77.3865.

[30] G. Kresse and D. Joubert, "From ultrasoft pseudopotentials to the projector augmented-wave method," *Physical Review B*, vol. 59, no. 3, pp. 1758–1775, 1999. DOI: 10.1103/PhysRevB.59.1758.

[31] L. Zhang, G. Csányi, E. van der Giessen, and F. Maresca, "Atomistic fracture in bcc iron revealed by active learning of gaussian approximation potential," *npj Computational Materials*, vol. 9, no. 217, 2023. DOI: 10.1038/s41524-023-01174-6.

[32] P. K. Nandi *et al.*, "Efficacy of surface error corrections to density functional theory calculations of vacancy formation energy in transition metals," *Journal of Physics: Condensed Matter*, vol. 22, no. 34, p. 345 501, 2010. DOI: 10.1088/0953-8984/22/34/345501. [Online]. Available: https://doi.org/10.1088/0953-8984/22/34/345501.

[33] H. J. Monkhorst and J. D. Pack, "Special points for brillouin-zone integrations," *Physical Review B*, vol. 13, no. 12, p. 5188, 1976.

[34] J. R. Rumble, Ed., *CRC Handbook of Chemistry and Physics*, 104th. Boca Raton, FL: CRC Press, 2023, Lattice parameter for α-Fe (bcc) taken from crystallographic tables, ISBN: 9781032353919. [Online]. Available: https://www.routledge.com/CRC-Handbook-of-Chemistry-and-Physics-104th-Edition/Rumble/p/book/9781032353919.

[35] Materials Project, *Materials data on fe (mp-13): Body-centered cubic iron*, https://legacy.materialsproject.org/materials/mp-13/, DFT-calculated properties using GGA-PBE: lattice constant, magnetic moment, FM–NM energy difference, 2024. [Online]. Available: https://legacy.materialsproject.org/materials/mp-13/.

[36] H. Herper, E. Hoffmann, and P. Entel, "Ab initio full-potential study of the structural and magnetic phase stability of iron," *Physical Review B*, vol. 60, no. 6, p. 3839, 1999.

[37] J. Crangle and G. Goodman, "The magnetization of pure iron and nickel," *Proceedings of the Royal Society of London. Series A. Mathematical and Physical Sciences*, vol. 321, no. 1547, pp. 477–491, 1971.

[38] N. Marzari, D. Vanderbilt, A. De Vita, and M. Payne, "Thermal contraction and disordering of the al (110) surface," *Physical Review Letters*, vol. 82, no. 16, p. 3296, 1999.

[39] J. Nocedal and S. Wright, *Numerical optimization*. Springer Science & Business Media, 2006.

[40] C. D. Latham, S. Öberg, P. R. Briddon, and F. Louchet, "A pseudopotential density functional theory study of native defects and boron impurities in feal," *Journal of Physics: Condensed Matter*, vol. 18, pp. 8859–8876, 2006. DOI: 10.1088/0953-8984/18/39/007. [Online]. Available: https://doi.org/10.1088/0953-8984/18/39/007.

[41] D. J. M. King, S. C. Middleburgh, P. A. Burr, T. M. Whiting, P. C. Fossati, and M. R. Wenman, "Density functional theory study of the magnetic moment of solute mn in bcc fe," *Physical Review B*, vol. 98, no. 2, p. 024 418, 2018. DOI: 10.1103/PhysRevB.98.024418.

Appendix

Appendix A: Quantum ESPRESSO Input Files

A.1 Bulk Ferromagnetic BCC Iron (1-atom primitive cell)

```
&control
    calculation = 'scf'
    verbosity = 'high'
    restart_mode= 'from_scratch'
    prefix = 'fe_bcc_fm_paw'
    outdir = './tmp'
    pseudo_dir = '../../../pseudopotentials'
    tprnfor = .true.
    tstress = .true.
    disk_io = 'low'
    wf_collect = .false.
    max_seconds = 82800
 /
&system
    ibrav = 3
    celldm(1) = 5.42
    nat = 1
    ntyp = 1

    ecutwfc = 90
    ecutrho = 1080

    occupations = 'smearing'
    smearing = 'mv'
    degauss = 0.01

    nspin = 2
    starting_magnetization(1) = 0.4
 /
&electrons
    electron_maxstep = 300
    conv_thr = 1e-10
    mixing_beta = 0.2
 /

ATOMIC_SPECIES
Fe 55.845 Fe.pbe-spn-kjpaw_psl.0.2.1.UPF

ATOMIC_POSITIONS (crystal)
Fe 0.0 0.0 0.0

K_POINTS (automatic)
```

```
  16 16 16 0 0 0
```

A.2 Vacancy Calculation (54-atom supercell)

```
&control
    calculation = 'relax'
    verbosity = 'high'
    restart_mode = 'from_scratch'
    prefix = 'fe_fm_vacancy_paw'
    outdir = './out'
    pseudo_dir = './pseudo'
    tprnfor = .true.
    tstress = .true.
    disk_io = 'none'
    wf_collect = .false.
    max_seconds = 140400
/
&system
    ibrav = 0
    nat = 53
    ntyp = 1
    ecutwfc = 90
    ecutrho = 1080
    occupations = 'smearing'
    smearing = 'mv'
    degauss = 0.01
    nspin = 2
    starting_magnetization(1) = 0.4
/
&electrons
    electron_maxstep = 300
    conv_thr = 1.0d-8
    mixing_beta = 0.2
/
&ions
    ion_dynamics = 'bfgs'
/
ATOMIC_SPECIES
    Fe  55.845  Fe.pbe-spn-kjpaw_psl.1.0.0.UPF
CELL_PARAMETERS angstrom
    8.60430000 0.00000000 0.00000000
    0.00000000 8.60430000 0.00000000
    0.00000000 0.00000000 8.60430000
ATOMIC_POSITIONS angstrom
    Fe  0.00000000 0.00000000 0.00000000
    Fe  1.43405000 1.43405000 1.43405000
    Fe  0.00000000 0.00000000 2.86810000
```

```
Fe  1.43405000 1.43405000 4.30215000
Fe  0.00000000 0.00000000 5.73620000
Fe  1.43405000 1.43405000 7.17025000
Fe  0.00000000 2.86810000 0.00000000
Fe  1.43405000 4.30215000 1.43405000
Fe  0.00000000 2.86810000 2.86810000
Fe  1.43405000 4.30215000 4.30215000
Fe  0.00000000 2.86810000 5.73620000
Fe  1.43405000 4.30215000 7.17025000
Fe  0.00000000 5.73620000 0.00000000
Fe  1.43405000 7.17025000 1.43405000
Fe  0.00000000 5.73620000 2.86810000
Fe  1.43405000 7.17025000 4.30215000
Fe  0.00000000 5.73620000 5.73620000
Fe  1.43405000 7.17025000 7.17025000
Fe  2.86810000 0.00000000 0.00000000
Fe  4.30215000 1.43405000 1.43405000
Fe  2.86810000 0.00000000 2.86810000
Fe  4.30215000 1.43405000 4.30215000
Fe  2.86810000 0.00000000 5.73620000
Fe  4.30215000 1.43405000 7.17025000
Fe  2.86810000 2.86810000 0.00000000
Fe  4.30215000 4.30215000 1.43405000
Fe  4.30215000 4.30215000 4.30215000
Fe  2.86810000 2.86810000 5.73620000
Fe  4.30215000 4.30215000 7.17025000
Fe  2.86810000 5.73620000 0.00000000
Fe  4.30215000 7.17025000 1.43405000
Fe  2.86810000 5.73620000 2.86810000
Fe  4.30215000 7.17025000 4.30215000
Fe  2.86810000 5.73620000 5.73620000
Fe  4.30215000 7.17025000 7.17025000
Fe  5.73620000 0.00000000 0.00000000
Fe  7.17025000 1.43405000 1.43405000
Fe  5.73620000 0.00000000 2.86810000
Fe  7.17025000 1.43405000 4.30215000
Fe  5.73620000 0.00000000 5.73620000
Fe  7.17025000 1.43405000 7.17025000
Fe  5.73620000 2.86810000 0.00000000
Fe  7.17025000 4.30215000 1.43405000
Fe  5.73620000 2.86810000 2.86810000
Fe  7.17025000 4.30215000 4.30215000
Fe  5.73620000 2.86810000 5.73620000
Fe  7.17025000 4.30215000 7.17025000
Fe  5.73620000 5.73620000 0.00000000
Fe  7.17025000 7.17025000 1.43405000
```

```
    Fe  5.73620000 5.73620000 2.86810000
    Fe  7.17025000 7.17025000 4.30215000
    Fe  5.73620000 5.73620000 5.73620000
    Fe  7.17025000 7.17025000 7.17025000
K_POINTS automatic
    10 10 10 0 0 0
```

A.3 K-point Convergence Test Example

```
&control
    calculation = 'scf'
    verbosity = 'high'
    restart_mode = 'from_scratch'
    prefix = 'fe'
    outdir = './out/'
    pseudo_dir = './pseudo'
    tprnfor = .true.
    tstress = .true.
    disk_io = 'none' ! Minimize disk usage, no restarts possible
    wf_collect = .false.
    max_seconds = 5400
/
&system
    ibrav = 0
    nat = 16
    ntyp = 1
    ecutwfc = 90
    ecutrho = 1080
    occupations = 'smearing'
    smearing = 'mv'
    degauss = 0.01
    nspin = 2
    starting_magnetization(1) = 0.4
/
&electrons
    electron_maxstep = 300
    conv_thr = 1.0d-8
    mixing_beta = 0.2
/
ATOMIC_SPECIES
Fe  55.845  Fe.pbe-spn-kjpaw_psl.1.0.0.UPF
ATOMIC_POSITIONS {angstrom}
Fe  0.00000000  0.00000000  0.00000000
Fe  1.43405000  1.43405000  1.43405000
Fe  0.00000000  0.00000000  2.86810000
Fe  1.43405000  1.43405000  4.30215000
Fe  0.00000000  2.86810000  0.00000000
```

```
Fe  1.43405000  4.30215000  1.43405000
Fe  0.00000000  2.86810000  2.86810000
Fe  1.43405000  4.30215000  4.30215000
Fe  2.86810000  0.00000000  0.00000000
Fe  4.30215000  1.43405000  1.43405000
Fe  2.86810000  0.00000000  2.86810000
Fe  4.30215000  1.43405000  4.30215000
Fe  2.86810000  2.86810000  0.00000000
Fe  4.30215000  4.30215000  1.43405000
Fe  2.86810000  2.86810000  2.86810000
Fe  4.30215000  4.30215000  4.30215000
K_POINTS {automatic}
  10 10 10 0 0 0
CELL_PARAMETERS {angstrom}
5.73620000 0.00000000 0.00000000
0.00000000 5.73620000 0.00000000
0.00000000 0.00000000 5.73620000
```

Appendix B: Convergence Test Data

Table 6: K-point convergence for all supercell sizes tested

Supercell	K-mesh	Energy (Ry/atom)	ΔE (meV/atom)
$1 \times 1 \times 1$	$16 \times 16 \times 16$	-329.26946887	—
$1 \times 1 \times 1$	$20 \times 20 \times 20$	-329.26942422	0.608
$1 \times 1 \times 1$	$24 \times 24 \times 24$	-329.26941565	0.117
$2 \times 2 \times 2$	$8 \times 8 \times 8$	-329.26946887	—
$2 \times 2 \times 2$	$10 \times 10 \times 10$	-329.26942422	0.608
$2 \times 2 \times 2$	$12 \times 12 \times 12$	-329.26941566	0.116
$3 \times 3 \times 3$	$6 \times 6 \times 6$	-329.26944329	—
$3 \times 3 \times 3$	$8 \times 8 \times 8$	-329.26941566	0.376
$3 \times 3 \times 3$	$10 \times 10 \times 10$	-329.26941865	0.041
$4 \times 4 \times 4$	$4 \times 4 \times 4$	-329.26946887	—
$4 \times 4 \times 4$	$6 \times 6 \times 6$	-329.26941566	0.724
$4 \times 4 \times 4$	$8 \times 8 \times 8$	-329.26942010	0.060

Appendix C: Data Processing Scripts

Note: The complete analysis code (900+ lines) and all computational scripts are available in the project repository at https://github.com/Chuval1/bcc-iron-vacancy-dft. Below are the key functions and algorithms used in this work.

C.1 Vacancy Formation Energy Calculation

```python
def calculate_formation_energy(e_vac, e_bulk, n_bulk=54):
    """
```

```
    Calculate vacancy formation energy using Zhang-Northrup formalism.

    Parameters:
    e_vac: Total energy of defect supercell (Ry)
    e_bulk: Total energy of bulk supercell (Ry)
    n_bulk: Number of atoms in bulk supercell

    Returns:
    e_form_ev: Formation energy (eV)
    """
    if e_vac is None or e_bulk is None:
        return None

    e_form_ry = e_vac - ((n_bulk - 1) / n_bulk) * e_bulk
    e_form_ev = e_form_ry * 13.6057039763  # Ry to eV conversion
    return e_form_ev

def extract_energy(filename):
    """Extract the total energy from a Quantum ESPRESSO output file."""
    try:
        with open(filename, 'r') as file:
            content = file.read()

        # Look for the final total energy line
        match = re.search(r'!\s+total energy\s+=\s+([-\d.]+)\s+Ry', content
    )
        if match:
            energy_ry = float(match.group(1))
            return energy_ry
        else:
            raise ValueError(f"Could not find total energy in {filename}")
    except FileNotFoundError:
        print(f"Warning: File not found: {filename}")
        return None
```

C.2 Magnetic Moment Analysis

```
def parse_atomic_positions_and_moments(filename):
    """Extract atomic positions and magnetic moments from a QE output file.
    """
    try:
        with open(filename, 'r') as file:
            content = file.read()
    except FileNotFoundError:
        return None, None, None, None

    # Extract cell parameters
    cell_match = re.search(r'CELL_PARAMETERS.*?\n(.*?)\n(.*?)\n(.*?)\n',
                           content, re.DOTALL)
    if cell_match:
        cell = []
        for i in range(1, 4):
```

```
            vector = cell_match.group(i).strip().split()
            cell.append([float(x) for x in vector])
        cell = np.array(cell)
    else:
        # Default cubic cell for 3x3x3 supercell
        cell = np.eye(3) * 8.604

    # Find the final atomic positions
    positions_pattern = r'ATOMIC_POSITIONS.*?\n(.*?)(?:\n\n|\nEnd)'
    all_positions = re.findall(positions_pattern, content, re.DOTALL)

    if not all_positions:
        return None, None, None, None

    # Use the last set of positions (final relaxed structure)
    positions_text = all_positions[-1]
    atoms, positions = [], []

    for line in positions_text.strip().split('\n'):
        parts = line.split()
        if len(parts) >= 4 and parts[0] in ['Fe', 'Fe1', 'Fe2']:
            atoms.append('Fe')
            x, y, z = float(parts[1]), float(parts[2]), float(parts[3])
            positions.append([x, y, z])

    positions = np.array(positions)

    # Find magnetic moments
    moment_pattern = r'Magnetic moment per site.*?\n(.*?)(?:End of|\\n\\n)'
    moment_matches = re.findall(moment_pattern, content, re.DOTALL)

    moments = []
    if moment_matches:
        moment_text = moment_matches[-1]
        for line in moment_text.strip().split('\n'):
            if "atom" in line and "magn" in line:
                parts = line.split()
                if len(parts) >= 5:
                    moments.append(float(parts[-1]))

    return np.array(atoms), positions, np.array(moments), cell
```

C.3 Displacement Field Analysis

```
def identify_vacancy_position(bulk_positions, vac_positions,
    lattice_constant):
    """Identify the vacancy position by finding the missing atom."""
    if bulk_positions is None or vac_positions is None:
        return None

    # Find which atom is missing by checking distances
    vacancy_candidates = []
```

```
    for bulk_pos in bulk_positions:
        min_dist = float('inf')
        for vac_pos in vac_positions:
            dist = np.linalg.norm(bulk_pos - vac_pos)
            if dist < min_dist:
                min_dist = dist

        # If no atom within 1 Angstrom, this is likely the vacancy position
        if min_dist > 1.0:
            vacancy_candidates.append(bulk_pos)

    if vacancy_candidates:
        return vacancy_candidates[0]
    else:
        return np.mean(bulk_positions, axis=0)

def calculate_displacement_vectors(bulk_positions, vac_positions):
    """Calculate displacement vectors for matched atoms."""
    matches = match_atoms_between_structures(bulk_positions, vac_positions)

    displacements = []
    for _, row in matches.iterrows():
        bulk_idx = int(row['bulk_index'])
        vac_idx = int(row['vac_index'])

        bulk_pos = bulk_positions[bulk_idx]
        vac_pos = vac_positions[vac_idx]
        displacement = vac_pos - bulk_pos

        displacements.append({
            'bulk_index': bulk_idx,
            'vac_index': vac_idx,
            'bulk_position': bulk_pos,
            'vac_position': vac_pos,
            'displacement': displacement,
            'displacement_magnitude': np.linalg.norm(displacement)
        })

    return pd.DataFrame(displacements)
```

C.4 Main Analysis Pipeline

```
def main():
    """Main analysis function."""
    results = {}

    # Process both PAW and USPP
    for pp_type in ['PAW', 'USPP']:
        paths = PATHS[pp_type]

        # Extract energies from SCF calculations
```

```
        bulk_energy = extract_energy(paths['bulk_scf'])
        vac_energy = extract_energy(paths['vac_scf'])

        # Calculate formation energy
        formation_energy = calculate_formation_energy(vac_energy,
    bulk_energy)

        # Parse atomic positions and moments from relaxed structures
        bulk_data = parse_atomic_positions_and_moments(paths['bulk_relax'])
        vac_data = parse_atomic_positions_and_moments(paths['vac_relax'])

        if bulk_data[0] is not None and vac_data[0] is not None:
            bulk_atoms, bulk_positions, bulk_moments, bulk_cell = bulk_data
            vac_atoms, vac_positions, vac_moments, vac_cell = vac_data

            # Calculate structural properties
            vacancy_pos = identify_vacancy_position(bulk_positions,
                                                    vac_positions,
                                                    LATTICE_CONSTANT)
            displacements = calculate_displacement_vectors(bulk_positions,
                                                           vac_positions)

            # Store results
            results[pp_type] = {
                'formation_energy': formation_energy,
                'bulk_energy': bulk_energy,
                'vac_energy': vac_energy,
                'bulk_positions': bulk_positions,
                'vac_positions': vac_positions,
                'bulk_moments': bulk_moments,
                'vac_moments': vac_moments,
                'vacancy_pos': vacancy_pos,
                'displacements': displacements,
                'avg_bulk_moment': np.mean(bulk_moments),
                'avg_vac_moment': np.mean(vac_moments),
                'max_displacement': displacements['displacement_magnitude'
    ].max(),
                'mean_displacement': displacements['displacement_magnitude'
    ].mean()
            }

    # Generate plots and analysis
    create_comparison_plots(results)
    create_summary_table(results)

if __name__ == "__main__":
    main()
```

Appendix D: Computational Details

D.1 Computational Resources

- Memory per calculation: 500 GB
- Number of processors: 128 MPI tasks
- K-point parallelization: 8 pools (-nk 8)
- Computational facility: Hábrók HPC cluster

D.2 Software Versions

- Quantum ESPRESSO: 7.3.1-foss-2023a
- Python: 3.10.8-GCCcore-12.2.0
- SciPy-bundle: 2022.05-foss-2022a (includes NumPy, SciPy, pandas)
- Matplotlib: 3.5.2-foss-2022a
- PyYAML: 6.0-GCCcore-12.2.0
- Compiler toolchain: foss-2022a/2023a

D.3 Pseudopotential Files

- PAW: Fe.pbe-spn-kjpaw_psl.1.0.0.UPF
- USPP: Fe.pbe-spn-rrkjus_psl.0.2.1.UPF
- Alternative PAW: Fe.pbe-spn-kjpaw_psl.0.2.1.UPF

D.4 Parallelization Strategy

- Pure MPI parallelization (OMP_NUM_THREADS=1)
- K-point pools: 8 (16 k-points per pool for 10×10×10 mesh)
- MPI tasks per atom: ∼2.4 (128 tasks / 53-54 atoms)
- No OpenMP threading to avoid memory contention

Appendix E: Code and Data Availability

All computational input files, analysis scripts, and processed data used in this research are publicly available in the project repository:

https://github.com/Chuval1/bcc-iron-vacancy-dft